Inverted-region electron transfer as a mechanism for enhancing photosynthetic solar energy conversion efficiency

Hiroki Makita[a] and Gary Hastings[a,1]

[a]Department of Physics and Astronomy, Georgia State University, Atlanta, GA 30303

Edited by Gregory D. Scholes, Princeton University, Princeton, NJ, and accepted by Editorial Board Member Richard Eisenberg July 20, 2017 (received for review March 29, 2017)

In all photosynthetic organisms, light energy is used to drive electrons from a donor chlorophyll species via a series of acceptors across a biological membrane. These light-induced electron-transfer processes display a remarkably high quantum efficiency, indicating a near-complete inhibition of unproductive charge recombination reactions. It has been suggested that unproductive charge recombination could be inhibited if the reaction occurs in the so-called inverted region. However, inverted-region electron transfer has never been demonstrated in any native photosynthetic system. Here we demonstrate that the unproductive charge recombination in native photosystem I photosynthetic reaction centers does occur in the inverted region, at both room and cryogenic temperatures. Computational modeling of light-induced electron-transfer processes in photosystem I demonstrate a marked decrease in photosynthetic quantum efficiency, from 98% to below 72%, if the unproductive charge recombination process does not occur in the inverted region. Inverted-region electron transfer is therefore demonstrated to be an important mechanism contributing to efficient solar energy conversion in photosystem I. Inverted-region electron transfer does not appear to be an important mechanism in other photosystems; it is likely because of the highly reducing nature of photosystem I, and the energetic requirements placed on the pigments to operate in such a regime, that the inverted-region electron transfer mechanism becomes important.

electron transfer | inverted region | photosynthesis | photosystem I

In oxygen-evolving photosynthetic organisms (plants, algae, and cyanobacteria), solar energy is captured and converted independently in two large membrane-spanning protein complexes called photosystem I and photosystem II (PSI and PSII) (1). In both systems light induces the transfer of electrons from a chlorophyll donor species, via a series of protein-bound pigments, across a biological membrane. This transport of electrons across a biological membrane is the basic mechanism underlying solar energy capture and storage in all photosynthetic organisms. In PSI and PSII the photosynthetic electron-transfer (ET) processes have a remarkably high quantum efficiency (2). In this article a mechanism that contributes to this high efficiency is explored.

In this report we focus on ET processes that occur in isolated PSI photosynthetic reaction centers (RCs) from the cyanobacterium *Synechocystis* sp. PCC 6803 (S6803). The architecture of the protein-bound ET cofactors (pigments) in cyanobacterial PSI is outlined in Fig. 1 (3, 4). The cofactor organization in PSI from plants is similar (5).

ET in PSI

The bioenergetics of light-induced ET in isolated PSI particles at both 298 and 77 K are discussed in *Bioenergetics in Isolated Photosystem I RCs at 298 and 77 K*, and are outlined in Fig. S1. Briefly, within ∼50 ps following light excitation the secondary radical pair state $P700^+A_{1A}^-/P700^+A_{1B}^-$ is formed. The charge-separated state is further stabilized by forward ET from A_{1A}^- and A_{1B}^- to F_X, and then onto F_A and F_B. In this article we focus on the unproductive ($P700^+A_{1A}^- \rightarrow P700A_{1A}$) ET recombination reaction, with rate k_{0A} (Fig. 1), which competes with the forward ET process. The ($P700^+A_{1A}^- \rightarrow P700A_{1A}$) is the dominant charge recombination pathway at both 298 and 77 K (12, 13). Conclusions drawn for the ($P700^+A_{1A}^- \rightarrow P700A_{1A}$) recombination reaction will also apply to ($P700^+A_{1B}^- \rightarrow P700A_{1B}$) ET recombination, with rate k_{0B}, however. Often in the literature, the term A_1 refers to the secondary electron acceptor, which is a phylloquinone (PhQ) molecule in native PSI. In this article we will refer to binding site as A_1, and the quinone occupying the A_1 binding site will be referred to by name.

Inverted-Region ET

Marcus ET theory, in the classical or semiclassical limit, predicts a Gaussian dependence between ET rate and driving force (14). The ET rate increases with driving force until the reactions' reorganization energy matches the driving force. Further increase in the driving force leads to a nonintuitive decrease in ET rate, in the so-called inverted region where the reactions' reorganization energy is less than the driving force (see Fig. S2*A* in *Inverted-Region ET*).

Forward ET in PSI is highly efficient, with a quantum yield approaching unity (2). Such a high yield indicates a near-complete suppression of wasteful recombination reactions. One mechanism that might contribute to this suppression is to tune the ET energetics so that recombination occurs in the inverted region. This idea is outlined in Fig. S2*B*. In his Nobel lecture Marcus proposed that this inverted-region mechanism could be a factor contributing to the high quantum efficiency associated with solar energy conversion in photosynthetic systems (15). This idea has been further discussed by others (16).

Significance

Inverted-region electron transfer is widely suggested to be an important mechanism contributing to photosynthetic efficiency. However, this mechanism has never been demonstrated in any native photosynthetic system under physiological conditions. Here, inverted-region electron transfer is demonstrated in a native photosynthetic protein complex under physiological conditions. Furthermore, inverted-region electron transfer is shown quantitatively to be an important mechanism underlying the very high efficiency associated with solar energy conversion in photosystem I in situ.

Author contributions: H.M. and G.H. designed research; H.M. and G.H. performed research; G.H. contributed new reagents/analytic tools; H.M. and G.H. analyzed data; and H.M. and G.H. wrote the paper.

The authors declare no conflict of interest.

This article is a PNAS Direct Submission. G.D.S. is a guest editor invited by the Editorial Board.

[1]To whom correspondence should be addressed. Email: ghastings@gsu.edu.

This article contains supporting information online at www.pnas.org/lookup/suppl/doi:10.1073/pnas.1704855114/-/DCSupplemental.

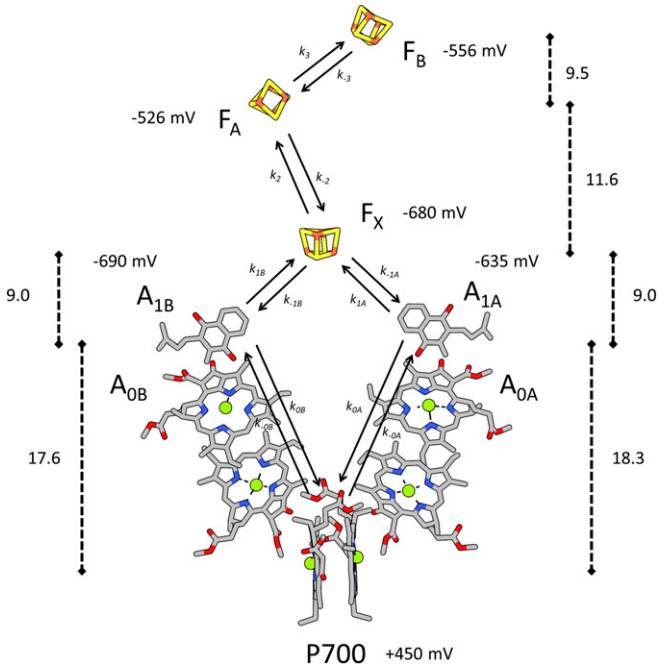

Fig. 1. Arrangement of the ET cofactors (pigments) in PSI with the two possible routes of ET indicated. Figure was derived from the 2.5-Å crystal structure of PSI from *Thermosynechococcus elongatus* (4). Cofactor hydrocarbon tails have been truncated. A similar figure is obtained using the 2.8-Å crystal structure of PSI from S6803 (3). Edge-to-edge distances (in angstrom) between cofactors (dotted) as well as the cofactor redox potentials for P700 (6), A_{1A} and A_{1B} (7), F_X (8), F_A and F_B (9, 10) are shown. Arrows indicate the kinetic model that was used previously to analyze the light-induced dynamics of radical pair states in PSI (7). $P700^+F_{A/B}^-$ and $P700^+F_X^-$ radical pair recombination proceeds via repopulation of A_1^- (11), as indicated.

The inverted-region effect has been confirmed experimentally, most notably by Miller and colleagues (16) and Miller et al. (17) for studies on synthetic systems. However, despite the recognition that inverted-region ET may play a role in promoting the high quantum yields associated with photosynthetic ET, there has never been any direct demonstration of an inverted-region ET process in any native photosynthetic RC under physiological conditions.

PSI Cofactor Modification

In recent years it has proven possible to incorporate a variety of quinones into the A_1 binding site in PSI particles with minimal disruption to the surrounding protein (7, 11, 18–20), and here we consider $P700^+A_1^-$ recombination in PSI with 10 different quinones incorporated (Table 1). Incorporation of different quinones allows easy modification of the driving force associated with ET (Fig. S1). By establishing ET rates and associated driving forces in PSI with the different quinones incorporated, a Marcus curve similar to that shown in Fig. S2*A* can be constructed, revealing where on the curve ET in the native system occurs.

ET in PSI with Foreign Quinones Incorporated

Recently, we have used time-resolved visible and infrared spectroscopy to study the bioenergetics of ET in PSI with eight different quinones incorporated, at both 298 and 77 K (7, 23). With the experimental data, kinetic modeling in combination with nonadiabatic ET theory was used to estimate the in situ midpoint potentials (E_m) for the different quinones (7, 23) (Tables 1 and 2). Here, these studies are extended to consider two additional quinones, AQS and DMNQ (2 and 3 in Tables 1 and 2), incorporated into PSI.

With the estimated midpoint potentials for the incorporated quinones, the free energy associated with each ET process can be calculated. In addition, the kinetic simulations allow for the calculation of intrinsic ET rates, which because of equilibration between states can differ significantly from the observed rates (10, 11). In this paper we calculate both the free energy and intrinsic ET rates for ET from A_{1A}^- to $P700^+$ at both 298 and 77 K. Using these parameters, we construct Marcus curves and show that ET associated with unproductive radical pair recombination occurs in the inverted region for all quinones incorporated. In particular, ET occurs well into the inverted region in native PSI at room temperature (RT). Following on from this, we present calculations which demonstrate that inverted-region ET is an important mechanism for greatly increasing photosynthetic efficiency in PSI in situ.

Results

Recently we have incorporated AQS and DMNQ (see Table 1 legend for abbreviations) into PSI. Fig. 2*A* shows transient absorption changes at 703 nm obtained using PSI with AQS and DMNQ incorporated at 77 K, along with corresponding data obtained previously using PSI with seven other quinones incorporated (23). Observed time constants (τ_{obs}) obtained from fitting the transient absorption data at 77 K are listed in Table 1. At 703 nm it is well known that the absorption change is due to the loss of P700 ground-state absorption (due to $P700^+$ formation) (24, 25), and that the temporal profiles of the absorption changes in Fig. 2*A* are associated with $P700^+A_{1A}^- \rightarrow P700A_{1A}$ recombination (13) (see *Bioenergetics in Isolated Photosystem I RCs at 298 and 77 K*). The change in the recombination rate with the different quinones incorporated into PSI is obvious in Fig. 2*A*.

Recently a kinetic modeling study, using the observed time constants calculated from transient absorption data as input, was undertaken to estimate the in situ midpoint potential (E_m) for eight different quinones incorporated into the A_1 binding site in PSI (7). Table 1 lists these in situ midpoint potentials along with data for PSI with AQS and DMNQ incorporated. In addition, Table 1 lists the in vitro midpoint potentials ($E_{1/2}$) for the different quinones (in dimethylformamide vs. standard hydrogen electrode).

Table 1. In vitro ($E_{1/2}$) and in situ (E_m) midpoint potentials (in millivolts) for 10 different quinones incorporated into PSI

	77 K				$\tau[P700^+A_{1A}^- \rightarrow P700A_{1A}]$	
	Q	$E_{1/2}$	E_m (A_{1A})	ΔG^0	τ_{obs}	τ_{int}
1	AQ	−576	−675	−1,125	797	540
2	AQS	−569	−665	−1,115	538	488
3	DMNQ	−501	−640	−1,090	391	383
4	PhQ	−465	−635	−1,085	366	365
5	2MNQ	−418	−580	−1,030	239	226
6	PQ_9	−369	−560	−1,010	200	193
7	2ClNQ	−225	−475	−925	114	109
8	2BrNQ	−225	−460	−910	94	100
9	Cl_2NQ	−60	−415	−865	78	80
10	Br_2NQ	−60	−395	−845	70	73

$E_{1/2}$ values are taken from refs. 21 and 22 and $E_m(A_{1A})$ are taken from ref. 7 (except for AQS and DMNQ). The native quinone in PSI is PhQ (listed as #4 in table). $-\Delta G^0 = -e(E_m - 450)$ is the free energy associated with $P700^+A_{1A}^-$ recombination, in milli electron volts. The observed time constants τ_{obs} (in microseconds) obtained from fitting transient absorption data at 77 K are taken from previous studies (7, 23) (except for AQS and DMNQ). The intrinsic time constants τ_{int} (in microseconds) were calculated from kinetic modeling as outlined in *Intrinsic ET Rates Calculated from Kinetic Modeling*. AQ, 9,10-anthraquinone; AQS, sodium anthraquinone-2-sulfonate, Br_2NQ, 2,3-dibromo-NQ; Cl_2NQ, 2,3-dichloro-NQ; DMNQ, 2,3-dimethyl-NQ; NQ, 1,4-naphthoquinone; PhQ, phylloquinone; PQ9, plastoquinone-9; 2BrNQ, 2-bromo-NQ; 2ClNQ, 2-chloro-NQ; 2MNQ, 2-methyl-NQ.

Table 2. Free energy associated with $P700^+A_{1A}^-$ recombination at 298 K (in milli electron volts) for PSI with 10 different quinones incorporated into the A_{1A} binding site

298 K			$\tau[P^+(F_{A/B}^-/A_{1A}^-) \rightarrow P(F_{A/B}/A_{1A})]$	$\tau[P^+A_{1A}^- \rightarrow PA_{1A}]$
Q		ΔG^0	τ_{obs}	τ_{int}
1	AQ	−1,125	>100	2,022
2	AQS	−1,115	551	1,768
3	DMNQ	−1,090	∼100	1,278
4	PhQ	−1,085	∼100	1,199
5	2MNQ	−1,030	14.4	625
6	PQ_9	−1,010	3.2	502
7	2ClNQ	−925	0.187	221
8	2BrNQ	−910	0.165	195
9	Cl_2NQ	−865	0.140	138
10	Br_2NQ	−845	0.124	122

Data were calculated using $-\Delta G^0 = -e(E_m - 450)$, using previously estimated E_ms (7). The time constants τ_{obs} (in milliseconds) are obtained from fitting the experimentally observed absorption changes at 703 nm, at 298 K, and are taken from ref. 23 (except for AQS and DMNQ). The intrinsic time constants τ_{int} (in microseconds) were calculated as outlined in *Intrinsic ET Rates Calculated from Kinetic Modeling*.

These $E_{1/2}$'s span a range of over 500 mV (Table 1) while the E_ms span a range of 280 mV (Table 1 and Fig. S1).

Based on the in situ midpoint potentials listed in Table 1, and taking into account a $P700^+/P700$ midpoint potential of +450 mV (6), the driving force associated with unproductive radical pair recombination reaction ($P700^+A_1^- \rightarrow P700A_1$) can be calculated. These calculated driving forces ($-\Delta G^0$) are listed in Table 1.

In a first simple analysis of the data listed in Table 1, we consider a plot of the experimentally observed ET rates at 77 K versus the driving force calculated directly from the quinone in vitro midpoint potentials (Fig. 2*B*). The plot in Fig. 2*B* makes no assumptions concerning any type of theory or kinetic model that may be appropriate. However, the data in Fig. 2*B* are well described by a parabolic function, suggesting that a theory that predicts such a parabolic dependence might be appropriate.

Previously we have used the kinetic model outlined in Fig. 1 to calculate the population evolution of the various radical states (7). By comparing the time constant associated with this population evolution to the experimentally observed time constant, the in situ midpoint potentials of the quinones incorporated into PSI were calculated (7). These calculations required the forward and backward intrinsic ET rates (k_n and k_{-n} in Fig. 1) as input. However, these intrinsic rates were never reported as the focus was on estimating in situ redox potentials. The intrinsic time constants, τ_{int}, are listed in Tables 1 and 2. Details of their calculation are outlined in *Intrinsic ET Rates Calculated from Kinetic Modeling*.

The two time constants (τ_{obs} and τ_{int}) are similar for PSI with all of the different quinones incorporated at 77 K, except for AQ and AQS (Table 1). This similarity is expected because forward ET from A_{1A}^- to F_X is thermodynamically uphill (and less likely to occur at 77 K), so $P700^+A_{1A}^-$ recombination will occur directly without equilibration between $P700^+A_{1A}^-$ and $P700^+F_X^-$ states. Differences in τ_{obs} and τ_{int} are expected for PSI with AQ and AQS incorporated, because these quinones have low potentials, and A_{1A}^- to F_X ET is thermodynamically favorable, so recombination will involve thermodynamically uphill ET from F_X^- back to A_1. For these reasons τ_{obs} and τ_{int} at 77 K are expected to differ for PSI with AQ and AQS incorporated.

Marcus Plot Associated with Radical Pair Recombination at 77 K

Fig. 3*A* shows a Marcus plot using the 77 K intrinsic ET rates and driving forces listed in Table 1. The data points in Fig. 3*A* lie on the fitted function because nonadiabatic ET theory was used to derive the rates and in situ potentials for the quinones incorporated (7). As outlined previously, for $P700^+A_{1A}^-$ recombination at 77 K, a reorganization energy of 660 meV was used (λ_3 in ref. 7), so the parabolic curve peaks at 660 meV, where the reorganization energy matches the driving force. We showed previously that the ET processes in PSI could not be adequately simulated if the reorganization energy was as high as 1,000 meV or as low as 400 meV (7).

As discussed in *Bioenergetics in Isolated Photosystem I RCs at 298 and 77 K*, $P700^+F_{A/B}^-$ recombination is characterized by a time constant of ∼80 ms for PSI with PhQ incorporated at RT (Fig. S1). This recombination occurs via repopulation of the A_1^- state. The actual time constant associated with $P700^+A_{1A}^-$ recombination at RT can be derived from the experimentally observed time constant only with the aid of kinetic modeling. The time constants derived

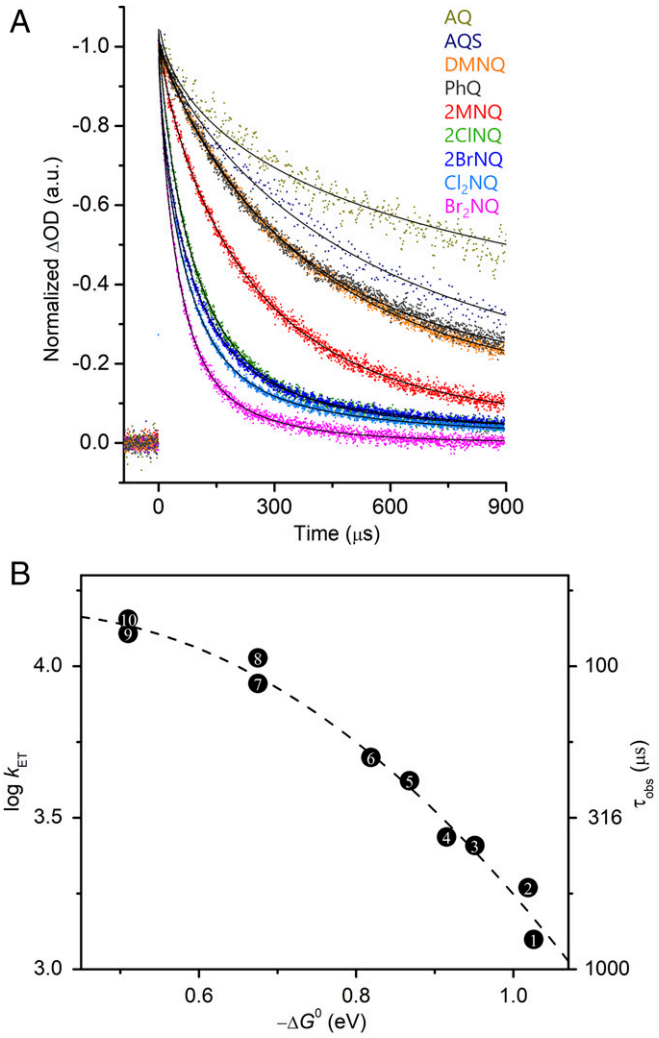

Fig. 2. (*A*) Flash-induced absorption changes at 703 nm (inverted) for PSI with 10 different quinones incorporated, at 77 K. Fitted functions are also shown (solid lines). (*B*) Plot of the observed $P700^+A_1^-$ recombination rate at 77 K versus the reaction free energy calculated using the quinone in vitro midpoint potentials [$-\Delta G^0 = -e(E_{1/2} - 450)$]. Data are fit to a parabolic function (dotted) and are numbered according to Table 1.

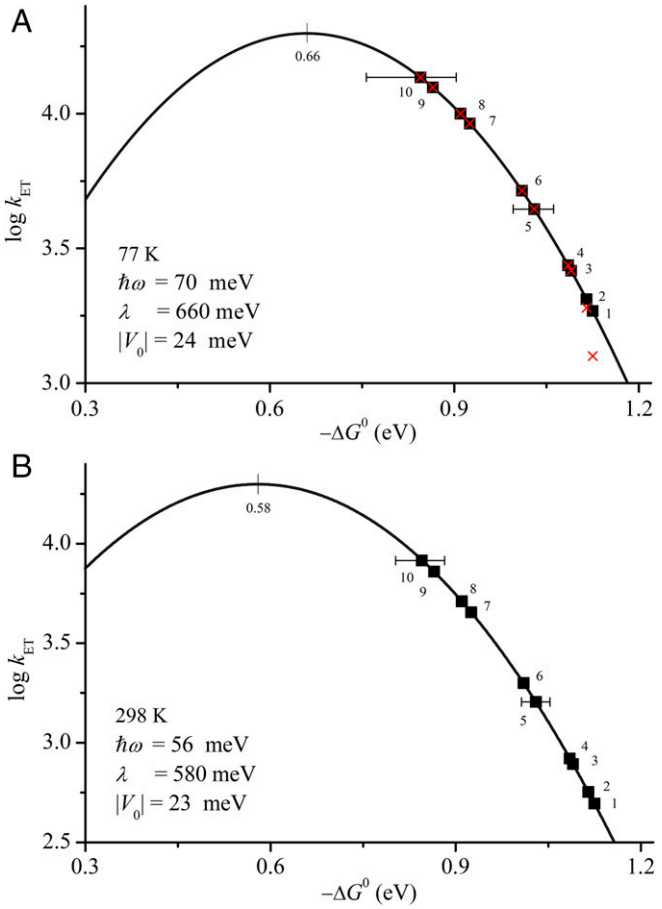

Fig. 3. (*A*) Marcus plot of $P700^+A_{1A}^-$ intrinsic (τ_{int}, ■) and observed (τ_{obs}, ×) recombination rates at 77 K versus the reaction free energy [$-\Delta G^0 = -e(E_m - 450)$] for 10 different quinones incorporated into PSI. Numbering is according to Table 1. The parabolic fitted function is based on ET parameters derived previously (7), along with the intrinsic time constants listed in Table 1. The horizontal error bars (items 5 and 10) are estimates of the in situ potential based on a possible ±0.2-Å error in the edge-to-edge distance between P700 and A_1. In the modeling, a reorganization energy of 660 meV and a mean vibrational mode with energy of 70 meV were used. (*B*) Marcus plot detailing $P700^+A_{1A}^-$ intrinsic recombination rates at 298 K versus the reaction free energy for 10 different quinones incorporated. The parabolic fitted function is based on ET parameters derived previously (7) along with the intrinsic time constants listed in Table 2. A reorganization energy of 580 meV and a mean vibrational mode with energy of 56 meV was used. A similar curve shifted vertically with the same peak position can be found for $P700^+A_{1B}^-$ recombination.

from modeling of RT data are listed in Table 2. For PSI with high potential quinones incorporated (quinones 7–10 in the tables) forward ET from A_1^- to F_X does not occur, and $P700^+A_1^-$ recombination occurs instead (12). So, for quinones 7–10 in Table 2 τ_{obs} and τ_{int} are similar. Fig. 3*B* shows a Marcus plot associated with $P700^+A_{1A}^-$ radical pair recombination at RT.

Discussion

In the past, radical pair recombination in photosynthetic RCs has often been suggested to occur in the inverted region (9, 14–16, 26, 27). This notion arises from considering the large free energy associated with such a recombination (Fig. S2*B*), which will likely be larger than the reorganization energy. That is, because radical pair recombination occurs in the inverted region, the thermodynamically downhill charge recombination pathway is effectively slowed, in turn ensuring the promotion of the less thermodynamically favorable forward ET pathway.

ET reactions in the purple bacterial photosynthetic RCs (PBRCs) have been by far the most widely studied (28), and it is primarily in connection with this system that the idea of inverted-region ET is considered (15, 16). However, in PBRCs the primary radical pair recombination reaction (so-called $P^+H_L^-$ recombination), at least for the native or wild-type (WT) system, is known not to occur in the inverted region (29–32). In fact, the unproductive $P^+H_L^-$ recombination reaction in WT PBRCs is nearly activationless (33). In PBRCs it appears to be the case that mechanisms related to protein relaxations in response to ET are (more) important in maximizing photosynthetic efficiency (29–32).

In the past, quinones have been incorporated into (very) harshly chemically pretreated PSI particles. This harsh procedure strips about 90% of the chlorophyll, lipids, and carotenoid molecules from the protein (34), leaving some doubts as to the integrity of the binding site surrounding the incorporated quinones. Nonetheless, for these harshly treated systems, it was demonstrated that the observed rate of the $P700^+F_{A/B}^-$ charge recombination at RT increased when higher potential quinones were incorporated (which decrease the reaction free energy associated with the $P700^+A_1^-$ recombination reaction) (27). At that time it was not known that ET in PSI was bidirectional, and kinetic modeling was not undertaken to establish the true (intrinsic) ET rates associated with $P700^+A_1^-$ recombination. Therefore, it could not be established if recombination in the native system occurred in the inverted region in these harshly treated photosynthetic proteins. Furthermore, to extract in situ redox potentials for the incorporated quinones in these harshly treated PSI particles, the data obtained were modeled assuming a fixed $P700^+A_1^-$ recombination rate for all of the different incorporated quinones. This assumption was necessary given the limited amount of experimental data available and the large number of parameters that had to be estimated in the kinetic model. However, this assumption implies that the inverted-region ET mechanism does not apply to the $P700^+A_1^-$ recombination reaction.

Here we provide unambiguous evidence (Fig. 3) supporting the notion that the unproductive $P700^+A_1^-$ radical pair recombination reaction in PSI, at both RT and LT, occurs in the inverted region. One could possibly argue about the precise values of the parameters involved in modeling the ET reactions outlined in Fig. 3. However, there is no reasonable scenario in which the parameters could be sufficiently altered that the data points (particularly data point 4 for PhQ, which represents the native system) in Fig. 3 could somehow be transferred from the right to the left side in the Marcus plots. The data plotted in Fig. 2 make no assumptions about any kind of applicable ET theory, and indicate that whatever theory may be appropriate, it will likely involve an inverted parabolic relation between the (logarithm of the) ET rate and reaction free energy, with all of the experimental data being to the right of the curve's peak. Nonadiabatic ET theory predicts exactly that.

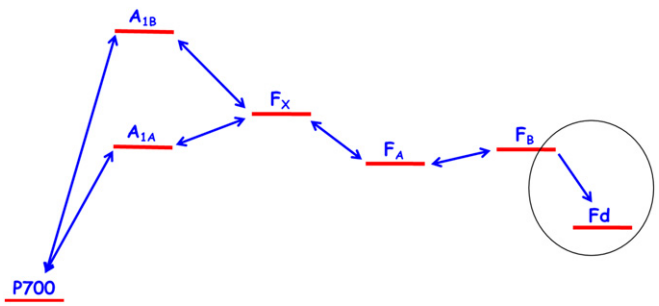

Fig. 4. Model used in kinetic simulations for PSI in situ. The circled region highlights the extension from previously considered kinetic models (7).

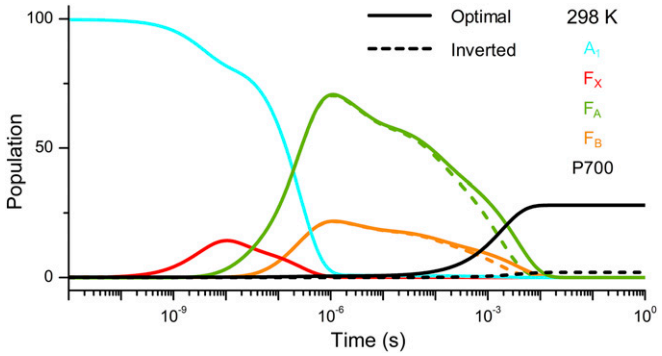

Fig. 5. Population dynamics of (A_{1A}^- + A_{1B}^-) (cyan), F_X^- (red), F_A^- (green), F_B^- (orange), and P700 (black) simulated using the first and second-order time constants and amplitudes associated with ET from F_B^- to Fd (see *Modeling ET from F_B^- to the Mobile Fd Electron Acceptor*). Dotted lines are for PSI where $P700^+A_{1A}^-$ and $P700^+A_{1B}^-$ radical pair recombination occur in the inverted region. Solid lines are for PSI where radical pair recombination is optimized by modifying the reorganization energy to match the free energy. In the inverted region the extent of recovery of P700 remains low (black, dotted) while it is considerably increased for the situation where the rate is optimized ($-\Delta G^0 = \lambda$) (black, solid).

Inverted-Region ET Is Necessary for High Photosynthetic Efficiency. The data presented here provide an unambiguous example of an unproductive ET recombination process in a native photosynthetic system under physiological conditions occurring in the inverted region (data point 4 in Fig. 3*B*). In our analysis of the bioenergetics in isolated PSI particles (7) we necessarily only considered ET to the iron–sulfur clusters and associated recombination reactions. In the thylakoid membranes of plants and bacteria, however, membrane-diffusible electron donors and acceptors are present that could impact radical pair recombination, and subsequently photosynthetic efficiency. An important question to address therefore is, to what extent inverted region ET could contribute to the high quantum efficiency of solar energy conversion observed for PSI in the thylakoid membrane, in the presence of diffusible electron donors and acceptors?

For PSI in situ (in the thylakoid membrane) electrons "drain" out of PSI via a diffusible Fd cofactor (35, 36). To account for this process here we consider the model outlined in Fig. 4 in which electrons can transfer (irreversibly) from F_B^- to Fd. The midpoint potentials of F_B and Fd are approximately −556 (10) and −420 (35) mV, respectively, and ET from Fd^- back to F_B is unlikely.

To assess the quantum efficiency of forward ET (loosely called photosynthetic efficiency), the extent of $P700^+$ rereduction (by charge recombination) is calculated. The less $P700^+$ that is rereduced, the greater the quantum efficiency of ET (greater photosynthetic efficiency). By comparing the extent of $P700^+$ rereduction in models where the charge recombination ET reaction is specified to be optimized ($-\Delta G^0 = \lambda$), or is in the inverted region ($-\Delta G^0 > \lambda$), we can assess to what extent the inverted region ET mechanism impacts photosynthetic efficiency.

The details of the calculations undertaken using the model outlined in Fig. 4 are discussed in *Modeling ET from F_B^- to the Mobile Fd Electron Acceptor*. The time evolution of the population of various radical pair states based on such calculations is outlined in Fig. 5.

For PSI in the presence of Fd, with inverted-region ET included, and given the time constants that govern ET from F_B^- to Fd (see *Modeling ET from F_B^- to the Mobile Fd Electron Acceptor*), we calculate that $P700^+$ rereduction occurs in ∼2% of the PSI particles (Fig. 5, dotted). The efficiency of solar energy conversion in PSI is therefore ∼98%.

To assess the importance of the inverted-region ET mechanism in modulating photosynthetic efficiency, we consider a hypothetical situation in which the ET from A_{1A}^- to $P700^+$ is optimal, with $-\Delta G^0 = \lambda$. To achieve this optimal condition, the reorganization energy (λ_2 in ref. 7) is set at 1.085 eV. At this reorganization energy, $A_{1A}^- \rightarrow P700^+$ proceeds with a time constant of 50.4 μs, and the overall $P700^+F_{A/B}^-$ by a time constant of 3.60 ms. Fig. 5 (solid lines) shows the population evolution of the various radical states under this condition. The data in Fig. 5 indicate that $P700^+$ rereduction occurs in 28% of the PSI particles when the $P700^+A_{1A}^-$ radical pair recombination is optimized. That is, the quantum efficiency for solar conversion in PSI drops to 72%. For reasons discussed in *Modeling ET from F_B^- to the Mobile Fd Electron Acceptor*, this is likely to be a best-case scenario. The results summarized in Fig. 5 demonstrate that A_1^- to $P700^+$ ET (for native PSI at RT in the presence of electron acceptors) has to occur in the inverted region for highly efficient solar energy conversion in PSI to occur.

We have also considered kinetic models that extend upon that shown in Fig. 4, in which electron donations to $P700^+$ are also included (Figs. S3–S5). These calculations are detailed in *Kinetic Models Including Membrane-Diffusible Electron Donors* and *Kinetic Model Including Secondary Electron Donors*. The overall result, however, is that these extended models do not significantly alter the calculated photosynthetic efficiency obtained using the model outlined in Fig. 4 (Tables S1–S3). Therefore, inverted-region ET from A_1^- to $P700^+$ (for native PSI at RT) is required for highly efficient solar energy conversion in PSI in the presence of diffusible electron donors and acceptors.

Comparison of ET Processes in Other Photosystems. The bioenergetic ET scheme for native PSI at RT (Fig. S1, *Left*) shows that forward ET from A_{1A}^- to F_X is slightly endergonic, while forward ET from A_{1B}^- to F_X is slightly exergonic. The recombination reaction is very highly exergonic. The corresponding ET scheme is very different in PBRCs, however, where forward ET from H_A^- to Q_A is highly exergonic (33) (see figure 1 in ref. 34 for a comparison of the bioenergetics in PBRCs and PSI). These differences in the energetics between PSI and PBRCs arise because the PSI ET cofactors are by necessity highly reducing. So, the different mechanisms involved in promoting high photosynthetic efficiency in PSI compared with purple bacteria may simply be a consequence of the requirement that PSI generate highly reducing species.

Materials and Methods

Growth of *menB*$^-$ mutant cyanobacterial cells from S6803, and preparation of trimeric PSI particles from the cells, are undertaken as described previously (37). Methods used for foreign quinone incorporation into the A_1 binding site in PSI are also as described previously (7, 11, 12, 23). RT (∼298 K) and LT (∼77 K) transient absorption data for *menB*$^-$ PSI with the different quinones incorporated were undertaken as described previously (7, 23). Here we include data for PSI with AQS and DMNQ incorporated into the A_1 binding site.

Previously, kinetic modeling in combination with nonadiabatic ET theory was used to calculate time constants associated with the population evolution of radical pair states (τ_{av}) for PSI with eight different quinones incorporated. By comparing the observed time constants (τ_{obs}) with the calculated time constants (τ_{av}), estimates of the midpoint potential (E_m) of the different quinones incorporated into the protein binding site were made (7). The same procedures were applied here to estimate the midpoint potentials of AQS and DMNQ incorporated into PSI.

For the estimation of photosynthetic efficiency, the kinetic models were extended to include the diffusible electron donors and acceptors. Full details of all kinetic models and calculations are given in *Modeling ET from F_B^- to the Mobile Fd Electron Acceptor*, *Kinetic Models Including Membrane-Diffusible Electron Donors*, and *Kinetic Model Including Secondary Electron Donors*.

ACKNOWLEDGMENTS. We thank Marilyn Gunner and Stefano Santabarbara for fruitful discussions. G.H. thanks Maged Henary for synthesizing DMNQ. This article was made possible by a National Priorities Research Program Award (NPRP 4-183-1-034) from the Qatar National Research Fund (a member of The Qatar Foundation). H.M. acknowledges support from the Molecular Basis of Disease Program at Georgia State University. The statements made herein are solely the responsibility of the authors.

1. Walker D (1993) *Energy, Plants and Man* (Oxygraphics, Brighton, UK), 2nd Ed.
2. Sun ASK, Sauer K (1971) Pigment systems and electron transport in chloroplasts. I. Quantum requirements for the two light reactions in spinach chloroplasts. *Biochim Biophys Acta* 234:399–414.
3. Mazor Y, Nataf D, Toporik H, Nelson N (2013) Crystal structures of virus-like photosystem I complexes from the mesophilic cyanobacterium Synechocystis PCC 6803. *eLife* 3:e01496.
4. Jordan P, et al. (2001) Three-dimensional structure of cyanobacterial photosystem I at 2.5 A resolution. *Nature* 411:909–917.
5. Mazor Y, Borovikova A, Nelson N (2015) The structure of plant photosystem I supercomplex at 2.8 Å resolution. *eLife* 4:e07433.
6. Nakamura A, Suzawa T, Kato Y, Watanabe T (2011) Species dependence of the redox potential of the primary electron donor p700 in photosystem I of oxygenic photosynthetic organisms revealed by spectroelectrochemistry. *Plant Cell Physiol* 52:815–823.
7. Makita H, Hastings G (2016) Modeling electron transfer in photosystem I. *Biochim Biophys Acta* 1857:723–733.
8. Parrett KG, Mehari T, Warren PG, Golbeck JH (1989) Purification and properties of the intact P-700 and Fx-containing Photosystem I core protein. *Biochim Biophys Acta* 973:324–332.
9. Brettel K (1997) Electron transfer and arrangement of the redox cofactors in photosystem I. *Biochim Biophys Acta* 1318:322–373.
10. Santabarbara S, Heathcote P, Evans MCW (2005) Modelling of the electron transfer reactions in Photosystem I by electron tunnelling theory: The phylloquinones bound to the PsaA and the PsaB reaction centre subunits of PS I are almost isoenergetic to the iron-sulfur cluster F(X). *Biochim Biophys Acta* 1708:283–310.
11. Makita H, Zhao N, Hastings G (2015) Time-resolved visible and infrared difference spectroscopy for the study of photosystem I with different quinones incorporated into the A1 binding site. Biochim Biophys Acta, *Bioenerg* 1847:343–354.
12. Makita H, Hastings G (2015) Directionality of electron transfer in cyanobacterial photosystem I at 298 and 77K. *FEBS Lett* 589:1412–1417.
13. Srinivasan N, Golbeck JH (2009) Protein-cofactor interactions in bioenergetic complexes: The role of the A1A and A1B phylloquinones in Photosystem I. *Biochim Biophys Acta* 1787:1057–1088.
14. Marcus RA, Sutin N (1985) Electron transfers in chemistry and biology. *Biochim Biophys Acta* 811:265–322.
15. Marcus RA (1992) Electron transfer reactions in chemistry: Theory and experiment (Nobel lecture). *Chemistry* 1991-1995:69–92.
16. Closs GL, Calcaterra LT, Green NJ, Penfield KW, Miller JR (1986) Distance, stereoelectronic effects, and the Marcus inverted region in intramolecular electron transfer in organic radical anions. *J Phys Chem* 90:3673–3683.
17. Miller JR, Calcaterra LT, Closs GL (1984) Intramolecular long-distance electron transfer in radical anions. The effects of free energy and solvent on the reaction rates. *J Am Chem Soc* 106:3047–3049.
18. Johnson TW, et al. (2001) Recruitment of a foreign quinone into the A1 site of photosystem I. In vivo replacement of plastoquinone-9 by media-supplemented naphthoquinones in phylloquinone biosynthetic pathway mutants of Synechocystis sp. PCC 6803. *J Biol Chem* 276:39512–39521.
19. Pushkar YN, Golbeck JH, Stehlik D, Zimmermann H (2004) Asymmetric hydrogen-bonding of the quinone cofactor in photosystem I probed by C-13-labeled naphthoquinones. *J Phys Chem B* 108:9439–9448.
20. Mula S, et al. (2012) Incorporation of a high potential quinone reveals that electron transfer in Photosystem I becomes highly asymmetric at low temperature. *Photochem Photobiol Sci* 11:946–956.
21. Prince RC, Gunner MR, Dutton PL (1982) 1 - Quinones of value to electron-transfer studies: Oxidation–reduction potentials of the first reduction step in an aprotic solvent. *Function of Quinones in Energy Conserving Systems*, ed Trumpower BL (Academic, New York), pp 29–33.
22. Prince RC, Leslie Dutton P, Malcolm Bruce J (1983) Electrochemistry of ubiquinones: Menaquinones and plastoquinones in aprotic solvents. *FEBS Lett* 160:273–276.
23. Makita H, Hastings G (2016) Time-resolved visible and infrared absorption spectroscopy data obtained using photosystem I particles with non-native quinones incorporated into the A1 binding site. *Data Brief* 7:1463–1468.
24. Brettel K, Leibl W (2001) Electron transfer in photosystem I. *Biochim Biophys Acta* 1507:100–114.
25. Golbeck J, Bryant D (1991) *Photosystem I. Current Topics in Bioenergetics* (Academic, New York), Vol 16, pp 83–175.
26. Moser C, Dutton L (1996) Outline of theory of protein electron transfer. *Protein Electron Transfer*, ed Bendall DS (BIOS Scientific, Oxford), pp 1–18.
27. Iwaki M, Itoh S (1994) Reaction of reconstituted acceptor quinone and dynamic equilibration of electron-transfer in the photosystem-I reaction center. *Plant Cell Physiol* 35:983–993.
28. Moser CC, Keske JM, Warncke K, Farid RS, Dutton PL (1992) Nature of biological electron transfer. *Nature* 355:796–802.
29. Gibasiewicz K, et al. (2016) Weak temperature dependence of P (+) H A (-) recombination in mutant Rhodobacter sphaeroides reaction centers. *Photosynth Res* 128:243–258.
30. LeBard DN, Martin DR, Lin S, Woodbury NW, Matyushov DV (2013) Protein dynamics to optimize and control bacterial photosynthesis. *Chem Sci (Camb)* 4:4127–4136.
31. Wang H, et al. (2009) Unusual temperature dependence of photosynthetic electron transfer due to protein dynamics. *J Phys Chem B* 113:818–824.
32. Wang H, et al. (2007) Protein dynamics control the kinetics of initial electron transfer in photosynthesis. *Science* 316:747–750.
33. Gunner MR, Dutton PL (1989) Temperature and -deltaG° dependence of the electron transfer from BPh^- to Q_A in reaction center protein from Rhodobacter sphaeroides with different quinones as QA. *J Am Chem Soc* 111:3400–3412.
34. Itoh S, Iwaki M, Ikegami I (2001) Modification of photosystem I reaction center by the extraction and exchange of chlorophylls and quinones. *Biochim Biophys Acta* 1507:115–138.
35. Sétif P (2001) Ferredoxin and flavodoxin reduction by photosystem I. *Biochim Biophys Acta* 1507:161–179.
36. Setif P (2006) Electron transfer from the bound iron-sulfur clusters to ferredoxin/flavodoxin: Kinetic and structural properties of ferredoxin/flavodoxin reduction by photosystem I. *Photosystem I: The Light Driven Plastocyanin:Ferredoxin Oxidoreductase*, ed Golbeck J (Springer, Dordrecht, The Netherlands), pp 439–454.
37. Johnson TW, et al. (2000) Recruitment of a foreign quinone into the A(1) site of photosystem I. I. Genetic and physiological characterization of phylloquinone biosynthetic pathway mutants in Synechocystis sp. pcc 6803. *J Biol Chem* 275:8523–8530.
38. Hastings G, Hoshina S, Webber AN, Blankenship RE (1995) Universality of energy and electron transfer processes in photosystem I. *Biochemistry* 34:15512–15522.
39. Hastings G, Kleinherenbrink FA, Lin S, McHugh TJ, Blankenship RE (1994) Observation of the reduction and reoxidation of the primary electron acceptor in photosystem I. *Biochemistry* 33:3193–3200.
40. Webber AN, Lubitz W (2001) P700: The primary electron donor of photosystem I. *Biochim Biophys Acta* 1507:61–79.
41. Agalarov R, Brettel K (2003) Temperature dependence of biphasic forward electron transfer from the phylloquinone(s) A1 in photosystem I: Only the slower phase is activated. *Biochim Biophys Acta* 1604:7–12.
42. Schlodder E, Falkenberg K, Gergeleit M, Brettel K (1998) Temperature dependence of forward and reverse electron transfer from A1-, the reduced secondary electron acceptor in photosystem I. *Biochemistry* 37:9466–9476.
43. Marcus RA (1956) On the theory of oxidation-reduction reactions involving electron transfer. I. *J Chem Phys* 24:966–978.
44. Hopfield JJ (1974) Electron transfer between biological molecules by thermally activated tunneling. *Proc Natl Acad Sci USA* 71:3640–3644.
45. Moser CC, Chobot SE, Page CC, Dutton PL (2008) Distance metrics for heme protein electron tunneling. *Biochim Biophys Acta* 1777:1032–1037.
46. Sétif PQY, Bottin H (1994) Laser flash absorption spectroscopy study of ferredoxin reduction by photosystem I in Synechocystis sp. PCC 6803: Evidence for submicrosecond and microsecond kinetics. *Biochemistry* 33:8495–8504.
47. Hippler M, Drepper F (2006) Electron transfer between photosystem i and plastocyanin or cytochrome c6. *Photosystem I: The Light-Driven Plastocyanin:Ferredoxin Oxidoreductase*, ed Golbeck JH (Springer, Dordrecht, The Netherlands), pp 499–513.
48. Hope AB (2000) Electron transfers amongst cytochrome f, plastocyanin and photosystem I: Kinetics and mechanisms. *Biochim Biophys Acta* 1456:5–26.
49. Baymann F, Rappaport F, Joliot P, Kallas T (2001) Rapid electron transfer to photosystem I and unusual spectral features of cytochrome c(6) in Synechococcus sp. PCC 7002 in vivo. *Biochemistry* 40:10570–10577.
50. Metzger SU, Pakrasi HB, Whitmarsh J (1995) Characterization of a double deletion mutant that lacks cytochrome c6 and cytochrome M in Synechocystis 6803. *Photosynthesis: From Light to Biosphere*, ed Mathis P (Kluwer Academic, Dordrecht, The Netherlands), Vol 2, pp 823–826.
51. Hippler M, Drepper F, Haehnel W, Rochaix J-D (1998) The N-terminal domain of PsaF: Precise recognition site for binding and fast electron transfer from cytochrome c6 and plastocyanin to photosystem I of Chlamydomonas reinhardtii. *Proc Natl Acad Sci USA* 95:7339–7344.
52. Haehnel W, Ratajczak R, Robenek H (1989) Lateral distribution and diffusion of plastocyanin in chloroplast thylakoids. *J Cell Biol* 108:1397–1405.
53. Witt HT (1971) Coupling of quanta, electrons, fields, ions and phosphrylation in the functional membrane of photosynthesis. Results by pulse spectroscopic methods. *Q Rev Biophys* 4:365–477.
54. Joliot P, Joliot A (2006) Cyclic electron flow in C3 plants. *Biochim Biophys Acta, Bioenerg* 1757:362–368.
55. Vershubskii AV, Mishanin VI, Tikhonov AN (2014) Modeling of the photosynthetic electron transport regulation in cyanobacteria. *Biochem (Mosc) Supp Ser A Membr Cell Biol* 8:262–278.
56. Lee T-X, Metzger SU, Cho YS, Whitmarsh J, Kallas T (2001) Modification of inhibitor binding sites in the cytochrome bf complex by directed mutagenesis of cytochrome b6 in Synechococcus sp. PCC 7002. *Biochim Biophys Acta* 1504:235–247.